Ceramics International xxx (xxxx) xxx

Contents lists available at ScienceDirect

Ceramics International

journal homepage: www.elsevier.com/locate/ceramint

Fabrication and thermoelectric properties of multilayer textured Sr-doped $Ca_3Co_4O_9$/Ag laminar composites

P. Amirkhizi [a,*], M.A. Madre [b], H.C. Wang [c], Z.H. Li [c], M.A. Torres [b], A. Sotelo [b], M. Hedayati [a], A.V. Kovalevsky [a], Sh. Rasekh [a]

[a] Department of Materials and Ceramic Engineering, CICECO-Aveiro Institute of Materials, University of Aveiro, 3810-193, Aveiro, Portugal
[b] INMA (CSIC-Universidad de Zaragoza), M[a] de Luna, 3, 50018, Zaragoza, Spain
[c] School of Physics, State Key Laboratory of Crystal Materials, Shandong University, Jinan, 250100, PR China

ARTICLE INFO

Handling Editor: Dr P. Vincenzini

Keywords:
Multilayer $Ca_3Co_4O_9$/Ag composite
Hot-uniaxial pressing
TE properties

ABSTRACT

This work presents a comparative analysis of pure and Ag-intercalated $Ca_3Co_4O_9$ multilayer thermoelectric materials prepared through the hot-uniaxial pressing technique. Samples were prepared by attrition milling and hot-pressed at 900 °C and 55 MPa for 1 h. They were mirror polished, and some of them were stacked with and without intermediate Ag foil and hot-pressed again at 900 °C and 52 MPa for 1 h. Out-of-plane XRD showed that samples are nearly single-phase, and the grains are well oriented with their ab-plane perpendicular to the pressure direction. Microstructural studies confirmed perfect welding in the multilayer samples accompanied by the formation of a very thin layer containing larger grains and notable Ag diffusion close to the $Ca_3Co_4O_9$/Ag interface. Three-point bending stresses have been increased in Ag-containing samples, while microhardness has been raised in all samples hot-pressed twice. Thermoelectric measurements showed a decrease of thermal gradient along the Ag-containing sample, together with a drastic decrease of electrical resistivity when compared to the Ag-free ones. However, the Ag-layers have promoted a drastic decrease in the Seebeck coefficient, reflected in a notable reduction of the power factor of $Ca_3Co_4O_9$/Ag multilayer composites. Nevertheless, these results show that it is possible to use these materials to reduce Joule heating and increasing the compatibility with the welding compounds when building thermoelectric modules. Moreover, they open a new research line searching for larger S compounds to be intercalated with Ag foils.

1. Introduction

One of the most important problems humanity is facing today is related to the energy sector. Nowadays, scientists and society are claiming to reduce fossil fuels consumption to decrease the release of greenhouse gases to fight against global warming. Consequently, great efforts are made to develop more efficient systems for producing energy from renewable sources. However, most renewable energy comes from intermittent sources (solar, wind, hydroelectric, etc.), which are strongly dependent on the season, daytime, etc. Due to these constraints, fossil fuels are still necessary to fulfill the humanity's energy needs. Furthermore, the relatively low efficiency of energy conversion from these fossil fuels should also be considered, which results in heat losses of about 60 % of the initial energy. Consequently, until renewable energies can fully meet human needs, recovering this waste heat and converting it into useable electric power is of utmost importance. By doing so, it will allow enhancing the fossil fuels efficiency and, reducing their impact on the global climate by decreasing their consumption.

Thermoelectric (TE) modules can be used to generate useful electric power from renewable sources (sun, geothermal, etc.) or through waste heat harvesting in industrial processes [1–4]. The power these modules can produce and their efficiency, are related to the thermoelectric characteristics of each type of leg that forming the thermocouples [5] and their thermal and electrical contact resistances [6]. Nowadays, most of the commercial modules are using intermetallic compounds as legs, as they display high thermoelectric performances [7,8], evaluated by their figure-of-merit, ZT, which is defined as [9]:

$$ZT = TS^2\sigma/\kappa$$

Where T is the absolute temperature, S is Seebeck coefficient, and σ, and κ are electrical and thermal conductivities, respectively.

* Corresponding author.
E-mail address: parisa.amirkhizi@ua.pt (P. Amirkhizi).

https://doi.org/10.1016/j.ceramint.2024.09.030
Received 13 May 2024; Received in revised form 24 June 2024; Accepted 3 September 2024
Available online 3 September 2024

However, the traditional thermoelectric materials also present notable drawbacks including relatively low chemical stability under air [3], together with their scarcity, high costs, and the presence of heavy and toxic elements [8,10–13]. The potential to overcome those drawbacks was demonstrated by the discovery of promising TE characteristics in Na_xCoO_2 [14], with p-type conduction. This report spurred intense research on these CoO-based materials, leading to the discovery of new materials, such as $Ca_3Co_4O_9$ [15], which is considered one of the most promising p-type materials due to its relatively large TE performance among TE oxides. Moreover, it can work at high temperatures (up to ~ 800 °C) under air without degradation. On the other hand, its ZT values in bulk form are still far from those obtained in intermetallic compounds (typically >1 at T ≤ 500 °C) [8,16], limiting its conversion efficiency. Consequently, many efforts are made to optimize their TE performances using different approaches [17–20].

On the other hand, recently it has been reported a new multilayer $Bi_2Te_{2.79}Se_{0.21}$/Ag composite acting as single-leg, which leads to an increased power generation of about 4.2 times larger than that obtained in traditional single-leg TE modules using the same TE compound [21].

Consequently, a similar stack produced by alternating four hot-pressed $Ca_{0.93}Sr_{0.07}Co_4O_9$ ceramics, and three Ag-layers, has been studied in this work. This composition has been selected due to the high TE performances determined in hot-pressed compounds (ZT ~ 0.29) [22] Moreover, 1-layer and 4-layer hot-pressed samples without Ag, were also prepared in order to study the complete evolution of the TE properties. The structural and microstructural characteristics of 1-layer, 4-layer and 4-layer with Ag samples were compared and related to their TE performances. It should be highlighted that the material selection has not only been based in previous results obtained in this system [22–24], but also on its properties at temperatures relatively close to the Ag melting point to assure a good adhesion between Ag and the ceramic layers.

2. Experimental

The $Ca_{0.93}Sr_{0.07}Co_4O_9$ ceramic samples were prepared using appropriate amounts of $CaCO_3$ (≥99 %, Aldrich), $SrCO_3$ (≥98 %, Aldrich), and CoO (99.99 %, Aldrich) powders. They were mixed and attrition milled at 600 rpm for 1 h, in distilled water media, using zirconia balls. The water-based suspension was totally dried under IR radiation to obtain a very fine and soft light brown powder, which was subsequently calcined at 850 °C for 1 h. The resulting black powder was cold uniaxially pressed in the form of disks (25 mm Ø) under 250 MPa, followed by a hot-uniaxial-pressing process at 900 °C and 55 MPa for 1 h. In this process, two types of samples were processed: some were formed from 10 g of $Ca_{0.93}Sr_{0.07}Co_4O_9$ with 3.6 mm thickness, which was used as a reference, and others (4 g, and 1.5 mm thickness), which were processed into 4-layers stack. All these samples were cut into square shape (20 × 20 mm^2) and mirror polished. The square samples obtained from the 4 g ones, were stacked into a 4-layer structure with and without silver sheet (0.1 mm thickness, 99.95 %, Aldrich) and hot-pressed at 900 °C and 52 MPa for 1 h, producing samples with ~3.7 mm thickness in all cases. The structure of the stack with Ag, after the hot-pressing and cutting procedures, is shown in Fig. 1 for clarity. Finally, all samples were cut in the appropriate dimensions for their characterization.

Out-of-plane XRD analysis was performed on the surfaces perpendicular to the applied pressure direction for all samples in a PHILIPS X'PERT system with CuK_α radiation between 7 and 50° to determine the phase composition of the samples. Moreover, grain orientation has been estimated using Lotgering factor [25], taking the data for the randomly oriented grains from Ref. [26]. Microstructure has been studied in a Field Emission Scanning Electron Microscope (FESEM, Zeiss Merlin) on transversal polished and fractured sections of samples. Elemental analysis has been performed by an EDS device attached to the FESEM. Mechanical properties have been determined through the three-point bending test in an Instron 5565 machine with a 10 mm loading span fixture and a punch displacement speed of 30 μm/min, and Vickers microhardness using a Vickers indentation system (Matsuzawa MXT70) with 4.9 N applied load and 15 s dwell time. Electrical resistivity and Seebeck coefficient were measured simultaneously, using the standard DC four-probe technique and the steady state mode, in an LSR-3 system (Linseis GmbH) at 50–800 °C under He atmosphere. The measurements were performed using the surfaces perpendicular to the pressing direction. Taking the electrical resistivity and Seebeck coefficient data, the power factor ($PF = S^2/\rho$, where ρ is the electrical resistivity) has been calculated for all samples. Finally, charge carrier concentration and mobility at room temperature have been determined in all samples through Hall measurements in a L79/HCS system (Linseis GmbH) under air atmosphere.

3. Results and discussion

Fig. 2 presents the out-of-plane XRD patterns for all samples, between 5 and 50° for clarity. As can be observed in the plot, all samples show very similar patterns, and all the peaks correspond to the $Ca_3Co_4O_9$ phase, in agreement with previously published data [26,27]. Moreover, most of the peaks have been produced by (*00l*) reflections, indicating a high degree of grain orientation, with their c-axis quasi-perpendicular to the surface of the samples. In order to evaluate the grain orientation in the samples, the Lotgering factor has been

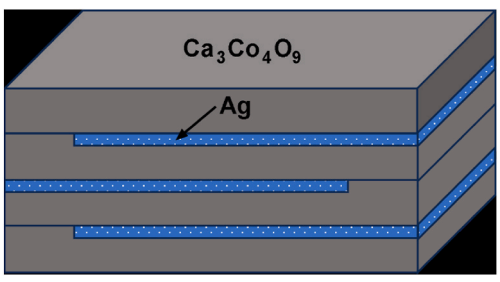

Fig. 1. Draw of the structure of the $Ca_3Co_4O_9$/Ag layered composite after the hot uniaxial pressing and cutting processes.

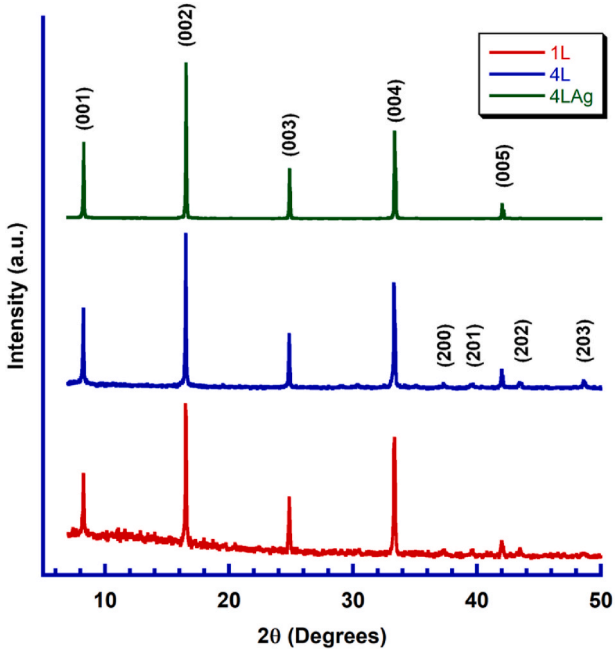

Fig. 2. Out-of-plane XRD patterns of all samples. The diffraction planes indicate the peaks associated to the $Ca_3Co_4O_9$ phase.

determined for all samples and the results are presented in Table 1. As it can be deduced from these data, the texture is drastically increasing from the samples with one hot-pressing process to those with two processes. This difference can be associated with the fact that the 4-layer samples should be welded with a second hot-pressing procedure, which induces a higher grain orientation. Moreover, when Ag-layers are intercalated between the $Ca_{0.93}Sr_{0.07}Co_4O_9$ ones, the texture is further enhanced, probably due to the Ag smoothness which can allow a better arrangement of the layers.

SEM micrographs taken on polished transversal surfaces of the 4-layer samples, without and with Ag-layers, are displayed in Fig. 3. The 4-layer samples without Ag show a very homogeneous microstructure and no evidence of the welding surfaces can be observed (Fig. 3a). The same situation is evidenced in Fig. 3b, where the Ag-layers are perfectly integrated in the samples microstructure. These features confirm that the hot-pressing procedure is adequate to produce very good welding between the different layers of the samples. Moreover, detailed analysis has shown that Ag-layer thickness has been decreased down to about 8 μm. This reduction can be associated not only with the Ag diffusion demonstrated in the next paragraph, but also with the plastic deformation of the whole composite under the hot-pressing conditions (900 °C and 52 MPa), which decreases its thickness and enhances its dimensions along the plane perpendicular to the applied pressure.

Fig. 4 displays a closer view of the $Ca_{0.93}Sr_{0.07}Co_4O_9$/Ag interface region. Linear EDS scanning performed perpendicularly to this region (indicated by the one-end arrow) has shown that Ag diffuses into the $Ca_{0.93}Sr_{0.07}Co_4O_9$ layer up to a distance of around 2 μm, as illustrated in the graph in Fig. 4. Silver also promotes the formation of a well-textured large-grained surface with around 8 μm, as shown by the vertical two-ends arrow in Fig. 4. This effect along the Ag surface has already been reported in similar systems, increasing the electrical conductivity [28]. On the other hand, the very small dimensions of these two zones (Ag diffusion, and textured zone) are only due to the very short time used in the hot-pressing process.

Fig. 5 presents the results of the three-point bending, and Vickers microhardness (HV) tests for all samples. From these data, it is clear that there is nearly no variation in the σ_{max} values between the Ag-free samples, while Ag is responsible for a significant increase in these values. This difference is due to the fact that Ag provides a plastic-flow region, and may resist crack propagation by deflecting them, as observed in similar systems [29]. On the other hand, the improvement is much lower than might be expected from these works, and this can be due to the presence of microcracks along the ab-planes, which can decrease mechanical properties without any significant effect on the transport ones. Moreover, these cracks tend to appear along the well-oriented and long grains, as previously reported for similar compounds [30]. As a consequence, these cracks appear close to the $Ca_3Co_4O_9$/Ag interface partially counterbalancing the improvements induced by Ag. In any case, the highest values obtained in Ag-intercalated samples (192 MPa) are about 15 % higher than those determined in Ag-free samples in this work. Moreover, they are much higher than those reported for sintered materials (20–125 MPa) [31,32], but lower than those obtained in textured materials produced through Spark Plasma Sintering (SPS) or by long hot-pressing processes (240–320 MPa) [31,33].

When observing the HV evolution in these samples, it is clear that the second hot-pressing process leads to a drastic increase, from 2.05 GPa for the 1-layer samples, to around 2.52 GPa for the 4-layer ones without Ag. This effect is associated with the larger grain sizes and better alignment obtained in samples subjected to two hot-pressing processes. These values are much higher than the reported in sintered (0.12–0.41 GPa) [31,32], or textured materials (1.30–1.55 GPa) [31,33].

Table 1
Lotgering factor of the different samples.

Sample	Lotgering factor
1-layer	0.849
4-layer	0.934
4-layer + Ag	0.986

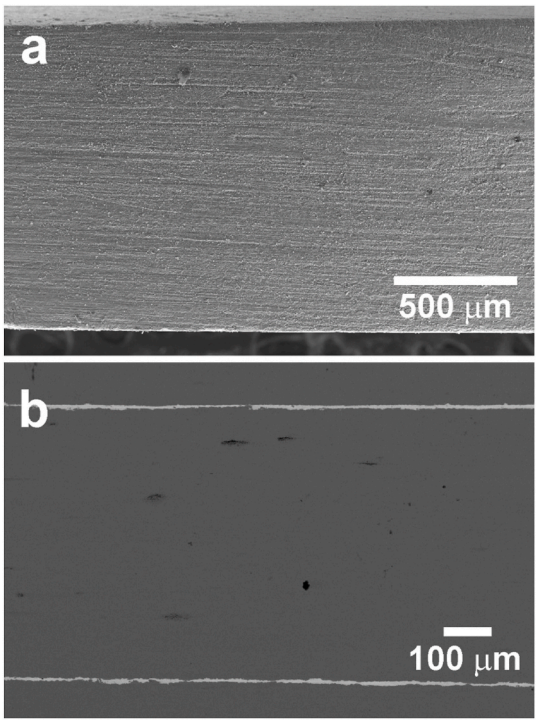

Fig. 3. SEM micrographs of transversal polished sections of: a) 4-layer sample; b) $Ca_{0.93}Sr_{0.07}Co_4O_9$/Ag sample, after the two hot-pressing processes.

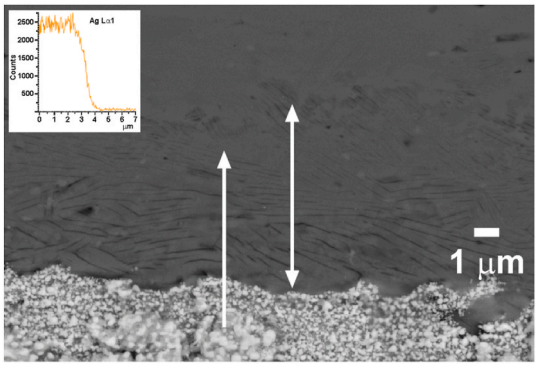

Fig. 4. Close view SEM micrograph of a transversal polished section of $Ca_{0.93}Sr_{0.07}Co_4O_9$/Ag sample, after the two hot-pressing processes, centered on the Ag/$Ca_{0.93}Sr_{0.07}Co_4O_9$ interface. The two-end arrow shows the thickness of the well-oriented-large grains region. The one-end arrow indicates the EDS measured line for Ag content, displayed in the insert.

The microstructural modifications observed in the SEM micrographs lead to significant changes of the thermal gradients along the samples observed during the thermoelectric characterization of samples, performed between 50 and 800 °C, and setting 30 °C constant thermal gradient between the two ends of the samples. The data have been recorded using two thermocouples in the central zone of the sample, with a span of 6 mm, and the results are presented in Fig. 6. As it can be easily observed in the graph, the thermal gradient is reduced for samples with two hot-pressing processes, when compared to those subjected to only one, due to their better grain orientation previously determined through their Lotgering factor. However, the presence of Ag clearly decreases the thermal gradient provided by the higher thermal

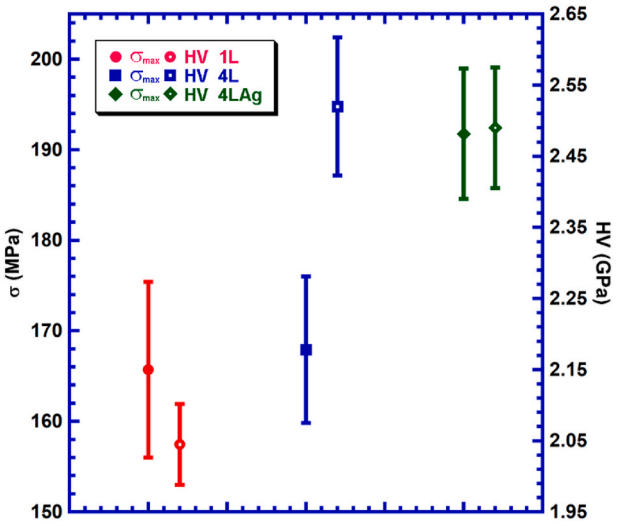

Fig. 5. Mechanical properties of the different samples determined through three-point bending tests, and Vickers microhardness, together with their respective measurement errors.

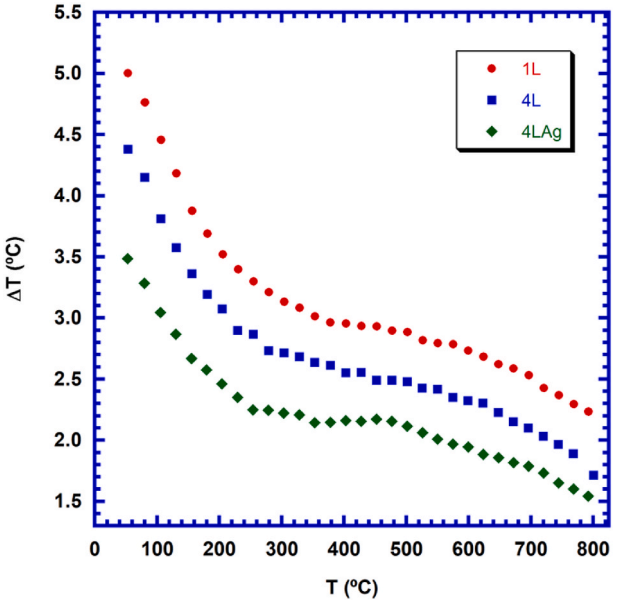

Fig. 6. Variation of the thermal gradient with temperature in all the samples in their central area with a distance between thermocouples of 6 mm, establishing a temperature difference of 30 °C between the ends of the samples.

conductivity of Ag, and that of the very well oriented and large grains region formed at the $Ca_{0.93}Sr_{0.07}Co_4O_9$/Ag interface. Consequently, it should be deduced that thermal conductivity should increase when the thermal gradient is decreasing.

Fig. 7a shows the electrical resistivity variation with temperature for all samples, together with relevant values extracted from the literature. In the graph, it is clear that the samples with the intercalated Ag-layers present much lower values than the other samples in the whole measured temperature range, which can be associated with the high electrical conductivity of Ag, and the well-aligned large grains in the region close to the $Ca_{0.93}Sr_{0.07}Co_4O_9$/Ag interface previously discussed. Moreover, it can also be affected by the very thin region close to the Ag-layers where Ag has diffused into the ceramic layer. On the other hand, electrical resistivity is only modified in the Ag-free samples at low temperatures, converging to the same values at high temperatures. This evolution clearly correlates with the different grain orientation between these samples previously discussed, and the possibility of lower grain orientation than the calculated in the inner part of these last samples. The minimum values determined in Ag-intercalated samples at 800 °C are around 1.8 mΩ cm, which is about 70 % lower than the values determined in Ag-free samples. Moreover, they are much lower than the best reported in the literature for textured compounds 6–25 mΩ cm [19,22,34–36], or sintered materials 9.5–14 mΩ cm [37–39].

This variation of electrical resistivity at room temperature for the different samples clearly agrees with the charge carrier concentration and mobility evolution displayed in Fig. 7b. As it can be observed in the graph, the mobility and carrier concentration are slightly decreased from 1-layer samples to the Ag-free 4-layer ones, and drastically raised for the Ag-intercalated ones. These variations in charge carrier concentration and mobility can be due to a possible lower grain orientation in the inner part of the samples, and the presence of the Ag-layers, respectively.

In Fig. 7c, the evolution of Seebeck coefficient (S) with temperature for all samples, together with relevant values extracted from the literature, is displayed. As it can be seen, S is positive at all temperatures, indicating a p-type conduction mechanism. Moreover, S increases with temperature in all Ag-free samples, which is the typical behavior in metals and degenerate semiconductors, when the charge carrier concentration, effective mass, and Fermi levels are constant with temperature [40]. However, the presence of Ag clearly modifies this tendency at temperatures below 300 °C. Furthermore, the plot clearly shows a drastic decrease in Seebeck coefficient values for the samples with Ag-layers in the whole measured temperature range, when compared to the other ones. This effect can be due to the same factors mentioned for the electrical resistivity section, which can increase the contribution of Ag to the Seebeck coefficient, making it lower than that of $Ca_{0.93}Sr_{0.07}Co_4O_9$. On the other hand, there is nearly no variation in S for the Ag-free samples due to their very similar microstructures, and much closer values of n and μ, when compared to the samples with Ag-layers. The highest S values for the Ag-intercalated samples at 800 °C are around 60 μV/K, which are about 70 % lower than the measured for Ag-free ones. Moreover, they are much lower than the best reported in the literature for textured materials 165–275 μV/K [19,22,34–36], or sintered specimens 182–200 μV/K [37–39].

Power factor evolution with temperature has been calculated for all samples, using the Seebeck coefficient and electrical resistivity values previously determined, and the results are illustrated in Fig. 7d, together with relevant values extracted from the literature. As it can be observed in the graph, the highest values have been obtained in the 4-layer Ag-free samples, with very similar PF values as the 1-layer ones, with a slight decrease at T > 550 °C due to their slightly lower S. On the contrary, the samples with intercalated Ag layers show a drastic decrease of PF in the whole measured temperature range provided by their extremely low S already discussed. The maximum PF values determined in Ag-intercalated samples at 800 °C (~0.2 mW/K^{2}m) are about 70 % lower than the obtained in Ag-free compounds. Moreover, they are much lower than the reported for textured materials 0.4–1.16 mW/K^{2}m [19,22,34–36], and close to the reported for sintered compounds 0.26–0.4 mW/K^{2}m [37–39].

These unexpected results, when considering the effect of the Ag-layers described in Ref. [21], can be associated with the thermal treatments performed on the samples, which are necessary to ensure good electrical connectivity between the different layers. Moreover, these thermal treatments have been performed at high temperatures (900 °C), with the consequent Ag diffusion inside the ceramic material, which was not the case in the results presented in Ref. [21]. However, these data point out to the possibility to produce large 349 samples by perfectly welding them through the hot-uniaxial pressing technique under suitable conditions. Furthermore, the presence of Ag leads to better mechanical properties and to the possibility to decrease the contact thermal and electrical resistances when integrating into thermoelectric modules.

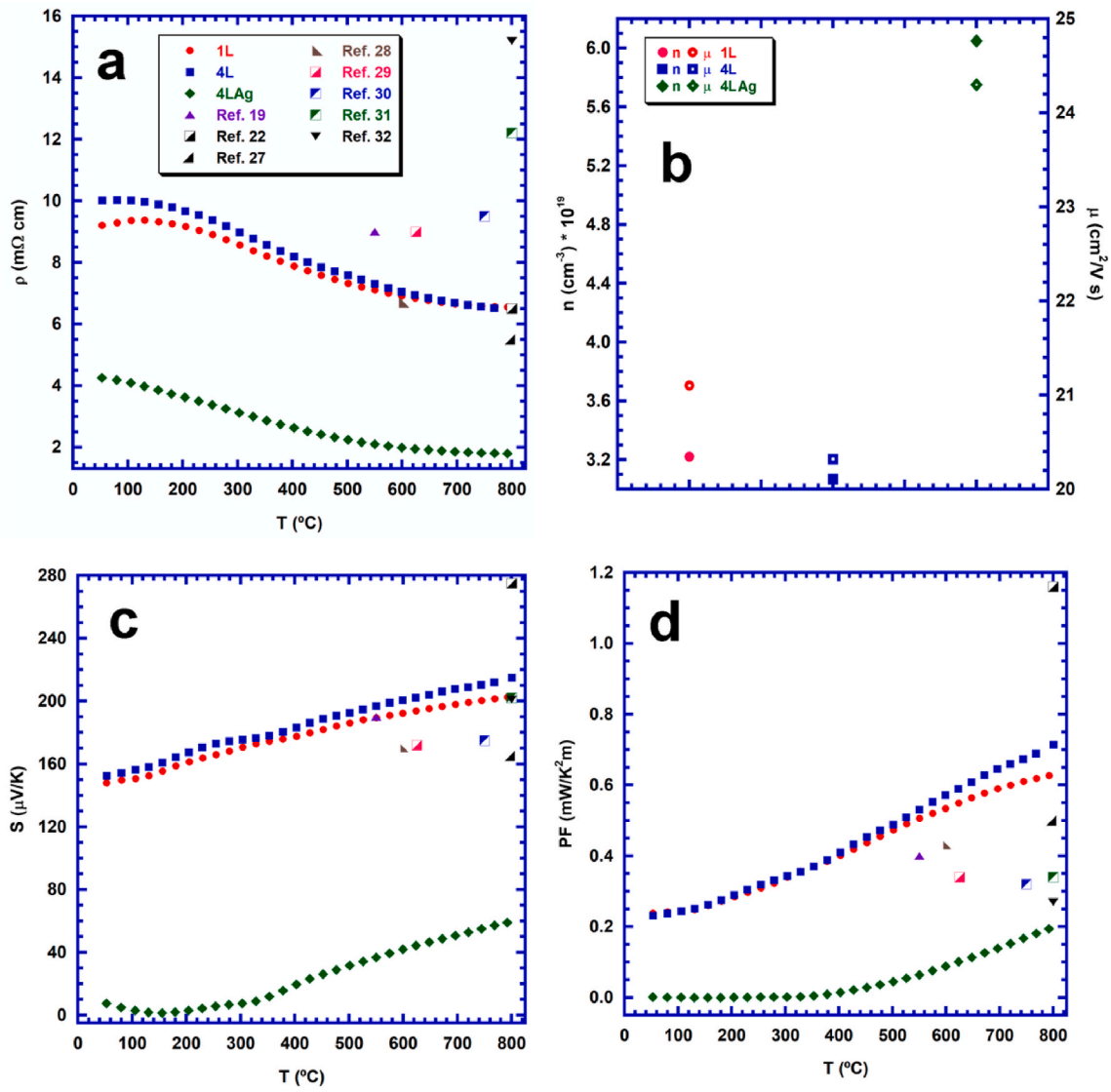

Fig. 7. Variation of several properties with temperature for all samples, together with relevant values presented in the literature. a) Electrical resistivity; b) room temperature charge carrier concentration and mobility; c) Seebeck coefficient; and d) power factor.

Additionally, the low resistivity would also decrease Joule heating, raising the module's performance.

4. Conclusions

In this work, pure and Ag-intercalated $Ca_3Co_4O_9$ multilayer thermoelectric materials have been successfully processed through the hot-uniaxial pressing technique. Samples were prepared from attrition milled precursors, which were cold pressed under 250 MPa, and hot-uniaxially pressed at 900 °C and 55 MPa for 1 h. The samples were mirror polished, and some of them were stacked as pure compounds while others were alternatively stacked with Ag foil, followed by hot-pressing at 900 °C and 52 MPa for 1 h. Out-of-plane XRD showed that samples were nearly single-phase, with well-oriented thermoelectric grains presenting their ab-plane perpendicular to the pressure direction, and a much higher Lotgering factor for samples hot-pressed twice, when compared to those pressed only once. Microstructural studies showed no significant differences between the 1-layer and 4-layer samples after the hot-pressing procedure. However, intercalated Ag-layers induced important microstructural modifications in the regions close to the $Ca_3Co_4O_9$/Ag interfaces. These modifications have been reflected in a decrease of the thermal gradient along these samples, when compared to the Ag-free ones. Three-point bending stress has been increased for 4-layer samples with Ag, while microhardness was raised for all 4-layer samples. Moreover, the electrical resistivity has been drastically decreased for Ag-containing samples, reaching 1.8 mΩ cm, which is around 70 % lower than the measured in Ag-free ones. On the other hand, S was reduced to 60 μV/K at 800 °C, about 70 % lower than the obtained in Ag-free samples. As a consequence, PF at 800 °C only reaches 0.2 mW/K^{2}m in Ag-containing samples, being about 70 % lower than those determined for Ag-free compounds, and fairly below the best reported values in the literature. However, these results show that it is possible to produce large $Ca_3Co_4O_9$ samples by perfectly welding them through the hot-uniaxial pressing technique under suitable conditions. The presence of Ag provides the decrease of the contact thermal and electrical resistances when integrating into thermoelectric modules. Additionally, the low resistivity would also decrease Joule heating, raising the module's performance. Finally, the results presented in this work open a new research direction, searching for an adequate dopant for the $Ca_3Co_4O_9$ compound which enhances its Seebeck coefficient without losing the high electrical conductivity of Ag-intercalated samples.

CRediT authorship contribution statement

P. Amirkhizi: Writing – review & editing, Writing – original draft, Methodology, Investigation. **M.A. Madre:** Validation, Software, Formal analysis, Data curation. **H.C. Wang:** Writing – review & editing, Software, Conceptualization. **Z.H. Li:** Writing – review & editing, Software, Conceptualization. **M.A. Torres:** Validation, Software. **A. Sotelo:** Writing – review & editing, Writing – original draft, Supervision, Resources, Methodology. **M. Hedayati:** Investigation, Data curation. **A.V. Kovalevsky:** Writing – review & editing, Supervision, Funding acquisition. **Sh. Rasekh:** Writing – review & editing, Supervision, Funding acquisition.

Declaration of competing interest

The authors declare that they have no known competing financial interests or personal relationships that could have appeared to influence the work reported in this paper.

Acknowledgements

The authors wish to thank the Gobierno de Aragón (Grupo de Investigacion T54_23R) and Universidad de Zaragoza (UZ2022-IAR-09) for financial support. Sh. Rasekh acknowledges the support of the Research Employment Contract FCT–CEECIND/02608/2017. This work was also developed within the scope of the PhD project of P. Amirkhizi (grant 2020.08051. BD funded by FCT) and the project CICECO-Aveiro Institute of Materials, UIDB/50011/2020, UIDP/50011/2020 & LA/P/0006/2020, financed by national funds through the FCT/MCTES (PIDDAC). Authors would like to acknowledge the use of Servicio General de Apoyo a la Investigación-SAI, Universidad de Zaragoza.

References

[1] L. Catalan, P. Alegria, M. Araiz, D. Astrain, Field test of a geothermal thermoelectric generator without moving parts on the Hot Dry Rock field of Timanfaya National Park, Appl. Therm. Eng. 222 (2023) 119843, https://doi.org/10.1016/j.applthermaleng.2022.119843.

[2] D. Champier, Thermoelectric generators: a review of applications, Energy Convers. Manag. 140 (2017) 167–181, https://doi.org/10.1016/j.enconman.2017.02.070.

[3] M.H. Elsheikh, D.A. Shnawah, M.F.M. Sabri, S.B.M. Said, M.H. Hassan, M.B. A. Bashir, M. Mohamad, A review on thermoelectric renewable energy: principle parameters that affect their performance, Renew. Sustain. Energy Rev. 30 (2014) 337–355, https://doi.org/10.1016/j.rser.2013.10.027.

[4] A.E. Risseh, H.P. Nee, O. Erlandsson, K. Brinkfeldt, A. Contet, F.F. Lng, G. Gaiser, A. Saramat, A. Saramat, T. Skare, S. Nee, J. Dellrud, Design of a thermoelectric generator for waste heat recovery application on a drivable heavy duty vehicle, SAE Int. J. Commer. Veh. 10 (2017) 26–44, https://doi.org/10.4271/2017-01-9178.

[5] G. Min, D.M. Rowe, in: D.M. Rowe (Ed.), CRC Handbook of Thermoelectrics, CRC Press, London, 1995.

[6] D.M. Rowe, G. Min, Evaluation of thermoelectric modules for power generation, J. Power Sources 73 (1998) 193–198, https://doi.org/10.1016/S0378-7753(97)02801-2.

[7] J.A. Santamaria, J. Alkorta, J.G. Sevillano, Microcompression tests of single-crystalline and ultrafine grain Bi_2Te_3 thermoelectric material, J. Mater. Res. 30 (2015) 2593–2604, https://doi.org/10.1557/jmr.2015.170.

[8] H. Wang, J. Hwang, M.L. Snedaker, I.-H. Kim, C. Kang, J. Kim, G.D. Stucky, J. Bowers, W. Kim, High thermoelectric performance of a heterogeneous PbTe nanocomposite, Chem. Mater. 27 (2015) 944–949, https://doi.org/10.1021/cm5042138.

[9] D.M. Rowe, in: D.M. Rowe (Ed.), Thermoelectrics Handbook: Macro to Nano, CRC Press, Boca Raton, FL (USA), 2006.

[10] A.C. Sklad, M.W. Gaultois, A.P. Grosvenor, Examination of $CeFe_4Sb_{12}$ upon exposure to air: is this material appropriate for use in terrestrial, high-temperature thermoelectric devices? J. Alloys Compd. 505 (2010) 6–9, https://doi.org/10.1016/j.jallcom.2010.05.167.

[11] A.A. Yaroshevsky, Abundances of chemical elements in the earth's crust, Geochem. Int. 44 (2006) 48–55, https://doi.org/10.1134/S001670290601006X.

[12] S. LeBlanc, Thermoelectric generators: linking material properties and systems engineering for waste heat recovery applications, Sust. Mater. Technol. 1–2 (2014) 26–35, https://doi.org/10.1016/j.susmat.2014.11.002.

[13] J. He, Y. Liu, R. Funahashi, Oxide thermoelectrics: the challenges, progress, and outlook, J. Mater. Res. 26 (2011) 1762–1772, https://doi.org/10.1557/jmr.2011.108.

[14] I. Terasaki, Y. Sasago, K. Uchinokura, Large thermoelectric power in $NaCo_2O_4$ single crystals, Phys. Rev. B 56 (1997) 12685–12687, https://doi.org/10.1103/PhysRevB.56.R12685.

[15] A.C. Masset, C. Michel, A. Maignan, M. Hervieu, O. Toulemonde, F. Studer, B. Raveau, J. Hejtmanek, Misfit-layered cobaltite with an anisotropic giant magnetoresistance: $Ca_3Co_4O_9$, Phys. Rev. B 62 (2000) 166–175, https://doi.org/10.1103/PhysRevB.62.166.

[16] H.C. Wang, J. Hwang, C. Zhang, T. Wang, W.B. Su, H. Kim, J. Kim, J.Z. Zhai, X. Wang, H. Park, W. Kim, C.L. Wang, Enhancement of the thermoelectric performance of bulk SnTe alloys via the synergistic effect of band structure modification and chemical bond softening, J. Mater. Chem. A 5 (2017) 14165–14173, https://doi.org/10.1039/C7TA03359A.

[17] A.K. Krolicka, M. Piersa, A. Mirowska, M. Michalska, Effect of sol-gel and solid-state synthesis techniques on structural, morphological and thermoelectric performance of $Ca_3Co_4O_9$, Ceram. Int. 44 (2018) 13736–13743, https://doi.org/10.1016/j.ceramint.2018.04.215.

[18] N. Wu, T.C. Holgate, N.V. Nong, N. Pryds, S. Linderoth, Effects of synthesis and spark plasma sintering conditions on the thermoelectric properties of $Ca_3Co_4O_{9+\delta}$, J. Electron. Mater. 42 (2013) 2134–2142, https://doi.org/10.1007/s11664-013-2546-7.

[19] J.G. Noudem, D. Kenfaui, D. Chateigner, M. Gomina, Toward the enhancement of thermoelectric properties of lamellar $Ca_3Co_4O_9$ by edge-free spark plasma texturing, Scripta Mater. 66 (2012) 258–260, https://doi.org/10.1016/j.scriptamat.2011.11.004.

[20] M.A. Torres, M.A. Madre, O.J. Dura, G. Garcia, S. Marinel, P. Martinez-Filgueira, A. Sotelo, Evaluation of pressure and temperature effect on the structure and properties of $Ca_{2.93}Sr_{0.07}Co_4O_9$ ceramic materials, Ceram. Int. 48 (2022) 7730–7747, https://doi.org/10.1016/j.ceramint.2021.11.321.

[21] X. Wang, H. Wang, W. Su, T. Wang, M.A. Madre, J. Zhai, T. Chen, A. Sotelo, C. Wang, A novel multilayer composite structured thermoelectric module with high output power, J. Mater. Chem. A 8 (2020) 3379–3389, https://doi.org/10.1039/C9TA13881A.

[22] M.A. Torres, F.M. Costa, D. Flahaut, K. Touati, Sh Rasekh, N.M. Ferreira, J. Allouche, M. Depriester, M.A. Madre, A.V. Kovalevsky, J.C. Diez, A. Sotelo, Significant enhancement of the thermoelectric performance in $Ca_3Co_4O_9$ thermoelectric materials through combined strontium substitution and hot-pressing process, J. Eur. Ceram. Soc. 39 (2019) 1186–1192, https://doi.org/10.1016/j.jeurceramsoc.2018.12.049.

[23] G. Constantinescu, Sh Rasekh, M.A. Torres, J.C. Diez, M.A. Madre, A. Sotelo, Effect of Sr substitution for Ca on the $Ca_3Co_4O_9$ thermoelectric properties, J. Alloys Compd. 577 (2013) 511–515, https://doi.org/10.1016/j.jallcom.2013.07.005.

[24] M.A. Torres, G. García, I. Urrutibeascoa, M.A. Madre, J.C. Diez, A. Sotelo, Fast preparation route to high-performances textured Sr-doped $Ca_3Co_4O_9$ thermoelectric materials through precursor powder modification, Sci. China Mater. 62 (2019) 399–406, https://doi.org/10.1007/s40843-018-9339-1.

[25] R. Furushima, S. Tanaka, Z. Kato, K. Uematsu, Orientation distribution–Lotgering factor relationship in a polycrystalline material—as an example of bismuth titanate prepared by a magnetic field, J. Ceram. Soc. Jpn. 118 (2010) 921–926, https://doi.org/10.2109/jcersj2.118.921.

[26] E. Woermann, A. Muan, Phase equilibria in the system CaO-cobalt oxide in air, J. Inorg. Nucl. Chem. 32 (1970) 1455–1459, https://doi.org/10.1016/0022-1902(70)80631-5.

[27] D. Sedmidubsky, V. Jakes, O. Jankovsky, J. Leitner, Z. Sofer, J. Hejtmanek, Phase equilibria in Ca-Co-O system, J. Solid State Chem. 194 (2012) 199–205, https://doi.org/10.1016/j.jssc.2012.05.014.

[28] Y. Feng, D.C. Larbalestier, Texture relationships and interface structure in Ag-sheathed Bi(Pb)-Sr-Ca-Cu-O superconducting tapes, Interface Sci. 1 (1993) 401–410, https://doi.org/10.1007/BF00188708.

[29] J. Joo, J.P. Singh, T. Warzynski, A. Grow, R.B. Poeppel, Role of silver addition on mechanical and superconducting properties of high-T_c superconductors, Appl. Supercond. 2 (1994) 401–410, https://doi.org/10.1016/0964-1807(94)90087-6.

[30] J.C. Diez, A. Sotelo, Sh Rasekh, H. Amaveda, M.A. Torres, P. Bosque, C. Chocarro, M.A. Madre, Composite Bi-2212/Ag superconductors grown by laser travelling floating zone at low rates, J. Supercond. Nov. Magnetism 28 (2015) 415–418, https://doi.org/10.1007/s10948-014-2758-y.

[31] D. Kenfaui, D. Chateigner, M. Gomina, J.G. Noudem, Texture, mechanical and thermoelectric properties of $Ca_3Co_4O_9$ ceramics, J. Alloys Compd. 490 (2010) 472–479, https://doi.org/10.1016/j.jallcom.2009.10.048.

[32] H. Amaveda, M. Mora, O.J. Dura, M.A. Torres, M.A. Madre, S. Marinel, A. Sotelo, Drastic enhancement of mechanical properties of $Ca_3Co_4O_9$ by B_4C addition, J. Eur. Ceram. Soc. 41 (2021) 402–408, https://doi.org/10.1016/j.jeurceramsoc.2020.08.024.

[33] D. Kenfaui, M. Gomina, D. Chateigner, J.G. Noudem, Mechanical properties of $Ca_3Co_4O_9$ bulk oxides intended to be used in thermoelectric generators, Ceram. Int. 40 (2014) 10237–10246, https://doi.org/10.1016/j.ceramint.2014.02.112.

[34] N.Y. Wu, T.C. Holgate, N.V. Nong, N. Pryds, S. Linderoth, High temperature thermoelectric properties of $Ca_3Co_4O_{9+\delta}$ by auto-combustion synthesis and spark plasma sintering, J. Eur. Ceram. Soc. 34 (2014) 925–931, https://doi.org/10.1016/j.jeurceramsoc.2013.10.022.

[35] H. Wang, X. Sun, X. Yan, D. Huo, X. Li, J.-G. Li, X. Ding, Fabrication and thermoelectric properties of highly textured $Ca_9Co_{12}O_{28}$ ceramic, J. Alloys Compd. 582 (2014) 294–298, https://doi.org/10.1016/j.jallcom.2013.07.145.

[36] D. Kenfaui, G. Bonnefont, D. Chateigner, G. Fantozzi, M. Gomina, J.G. Noudem, $Ca_3Co_4O_9$ ceramics consolidated by SPS process: optimisation of mechanical and thermoelectric properties, Mater. Res. Bull. 45 (2010) 1240–1249, https://doi.org/10.1016/j.materresbull.2010.05.006.

[37] F. Delorme, C. Fernandez Martin, P. Marudhachalam, D. Ovono Ovono, G. Guzman, Effect of Ca substitution by Sr on the thermoelectric properties of $Ca_3Co_4O_9$ ceramics, J. Alloys Compd. 509 (2011) 2311–2315, https://doi.org/10.1016/j.jallcom.2010.10.209.

[38] A.I. Klyndyuk, E.A. Chizhova, R.S. Latypov, S.V. Shevchenko, V.M. Kononovich, Effect of the addition of copper particles on the thermoelectric properties of the $Ca_3Co_4O_{9+\delta}$ ceramics produced by two-step sintering, Russ. J. Inorg. Chem. 67 (2022) 237–244, https://doi.org/10.1134/S0036023622020073.

[39] A.I. Klyndyuk, E.A. Chizhova, E.A. Tugova, R.S. Latypov, O.N. Karpov, M. V. Tomkovich, Thermoelectric multiphase ceramics based on layered calcium cobaltite, as synthesized using two-stage sintering, Glass Phys. Chem. 46 (2020) 562–569, https://doi.org/10.1134/S1087659620060127.

[40] D. Flahaut, J. Allouche, A. Sotelo, Sh Rasekh, M.A. Torres, M.A. Madre, J.C. Diez, Role of Ag in textured-annealed $Bi_2Ca_2Co_{1.7}O_x$ thermoelectric ceramic, Acta Mater. 102 (2016) 273–283, https://doi.org/10.1016/j.actamat.2015.09.036.